Physics of Fluids

RESEARCH ARTICLE | APRIL 12 2023

Investigation of motion characteristics of coarse particles in hydraulic collection

Ren Wan-Long (任万龙) ; Zhang Xu-Hui (张旭辉) ; Zhang Yan (张岩) ; Lu Xiao-Bing (鲁晓兵)

Physics of Fluids 35, 043322 (2023)
https://doi.org/10.1063/5.0142221

Physics of Fluids ARTICLE scitation.org/journal/phf

Investigation of motion characteristics of coarse particles in hydraulic collection

Cite as: Phys. Fluids **35**, 043322 (2023); doi: 10.1063/5.0142221
Submitted: 12 January 2023 · Accepted: 28 March 2023 ·
Published Online: 12 April 2023

Wan-Long Ren (任万龙),[1,2] Xu-Hui Zhang (张旭辉),[1,2] Yan Zhang (张岩),[1,a)] and Xiao-Bing Lu (鲁晓兵)[1,2]

AFFILIATIONS

[1]Institute of Mechanics, Chinese Academy of Sciences, Beijing 100190, China
[2]School of Engineering Science, University of Chinese Academy of Sciences, Beijing 100049, China

[a)]Author to whom correspondence should be addressed: zhangyan162@imech.ac.cn

ABSTRACT

The solid–fluid two-phase flow with coarse particles is an important research object in the two-phase transportation field, such as deep-sea mining. This paper adopts the resolved computational fluid dynamics-discrete element method to investigate the motion and mechanical characteristics of the coarse particles during the hydraulic collection. First, the rising process of coarse particles by combining the particle trajectory with the qualitative force analysis is analyzed during the hydraulic collection. The spiral phenomenon of the particle is found through the particle trajectory in numerical results, and the centripetal force is the reason for the spiral phenomenon of the particle. Second, the variations of the normalized fluid drag force and the rise time of particles are investigated at different fluid velocities and particle sizes. The results show that the rise of particles during hydraulic collection results from the rising and settling effects characterized by the fluid drag force and the relative gravity, respectively. Finally, appropriate particle size is recommended to save energy and improve the efficiency of hydraulic collection. In addition, the influence of the horizontal distance between coarse particles and the inlet of the suction pipe on particle rise is discussed.

I. INTRODUCTION

With the deepening of industrialization and the development of the world economy, the demand for mineral resources is increasing. The ocean contains a large number of resources, such as manganese nodules, gas and oil, gas hydrate, and various biological resources. Therefore, the rich resources of the ocean have attracted great interest and attention from all over the world.[1–4]

The collection of nodule particles is attracting increasing attention in the ocean. Many methods for collecting nodule particles, such as hydraulic collection methods, mechanical methods, and hybrid methods, have been developed. In 1978, the sea trial results of the Ocean Mining Incorporation (OMI) showed that the hydraulic collection methods were more efficient than other methods, environmentally friendly, and adapted to the complex marine environment.[5] The process of hydraulic collection is as follows: the nodule particles on the seabed were hydraulically sucked into the inlet of the pipe and then transported by pipe to the storage bin. Thus, the hydraulic collection is the first and key step to getting marine nodule particles. For this reason, it is necessary to investigate the motion and mechanical characteristics of nodule particles for efficiency and safety during hydraulic collection.

Then, researchers began to investigate the characteristics of particles in the hydraulic collection through experiments. Hong *et al.*[6] built a hybrid pickup device of nodule particles in a 2D flume tank to explore the factors affecting the efficiency of the hydraulic lifter, and the results showed the primary factors affecting the efficiency of the pickup device are the position and shape of the baffle plates. Yang and Tang[7] discussed the relationship between the efficiency of the picking devices and the main parameters, such as particles' size, shape, and parameters of the picking devices, through a large number of experiments, and found appropriate parameters could get an efficient collection rate. Zhao *et al.*[8] conducted hydraulic collection tests of spherical particles by changing the ratio of bottom clearance to the diameter of the particle and the diameter of the suction pipe to the diameter of the particle. They revealed the wake vortex could induce an unstable lift at the bottom and promote the particle rise. Chen *et al.*[9] analyzed the effects of particle density, size, and other factors on the flow field by particle image velocimetry (PIV) and obtained the influence laws of these parameters on the particle suction velocity. Zhang *et al.*[10] studied the critical suction velocity of particles through different kinds of experiments and revealed geometric similarity between the experimental model and engineering model with the same kind of material.

They also discussed the effects of dimensionless control parameters, such as the hydraulic collection number, the relative coarse particle diameter, the relative suction height, and the density ratio. Finally, they obtained a formula to predict the critical suction velocity of particles. Zhao *et al.*[11] investigated the performance characteristics of nodule pickup devices for hydraulic collection using spiral flow, and the difference between spiral flow and non-spiral flow was compared. They found using the spiral flow can increase the bottom clearance and suction force, and decrease the flow rate. Viggiano *et al.*[12] and Ali *et al.*[13] measured the cross-sectional volume fraction of the pipe using the advanced X-ray system and then studied the distribution characteristics of the solid–liquid two-phase flow. Although the relations between the collection efficiency of the pickup devices and related parameters have been revealed by a large number of experiments, the mechanical characteristics of particles are rarely discussed. That may be because the relevant physical quantities are difficult to obtain in experiments, such as the fluid drag force.

Compared with experimental research, numerical simulation can be easier to obtain the position and mechanical information of particles, such as particle velocity and fluid drag force.[14] In numerical simulation methods, the fluid is usually considered as the continuous phase. For particles, there are two methods. One is that particles are also considered as continuous phases in the Euler–Euler method, but it cannot characterize the continuous characteristics of particles.[15,16] The other is the Euler–Lagrange method, which treats particles as dispersed phases.[17–21] The motion and mechanical information of particles can be better obtained using the Euler–Lagrange method. Computational fluid dynamics (CFD) for the continuous phase and discrete element method (DEM) for the dispersed phase are combined to study solid–fluid two-phase flow, also known as the coupled CFD-DEM method.[22,23]

As shown in Fig. 1, the coupled CFD-DEM method can be divided into the unresolved and the resolved CFD-DEM methods by comparing the relative size of the mesh with particle.[24] For the unresolved CFD-DEM methods in Fig. 1(a), the particle size should be smaller than one-third of the mesh size.[25] For resolved CFD-DEM methods[26,27] in Fig. 1(b), the particle size should be more than eight times the mesh size, so the method is especially suitable for solving solid–fluid two-phase flow with large-size particles.[28] Hager *et al.*[29] proposed an optimized resolved CFD-DEM method based on fictitious domain method (FDM).[30,31] For the FDM, the void fraction of the mixture of particles and fluid is mapped onto the background mesh, and the velocity and force of boundary between the particles and the fluid are calculated by a gradient of the void fraction field.[32] Yu and Shao[33] verified the FDM through various typical particle flows, including the sedimentation of a circular particle and a sphere in a vertical pipe, the surrounding flow field, and the motion of a sphere in Poiseuille and Couette flows. They found the FDM is particularly neutral buoyant cases. Wang and Liu[34] developed a semi-resolved CFD-DEM method for wide particle sizes that combined resolved and unresolved CFD-DEM models, which still belonged to an unresolved CFD-DEM method.

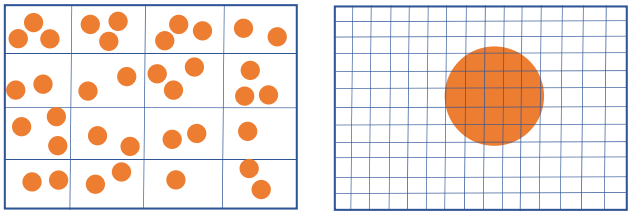

FIG. 1. Coupled CFD-DEM method: (a) unresolved CFD-DEM and (b) resolved CFD-DEM.

Nodule particles of the hydraulic collection are large and are still coarse particles even after crushing. Coarse particles refer to the ratio of particle diameter d_p to pipe diameter D greater than 0.1 (Ref. 14). To ensure the accuracy of the flow field, the mesh size cannot be too large, so the coarse particles have to occupy dozens or even thousands of meshes.[35] However, when the coarse particle size is much larger than the mesh, the unresolved CFD-DEM method is difficult to solve the problem, and the force of the fluid acting on the particles in the unresolved CFD-DEM method is obtained by the empirical force models. The empirical model is limited by many factors, such as the Reynolds number, which can lead to many unacceptable errors. The resolved CFD-DEM method for coarse particles can directly obtain the fluid–particle interaction force without using the empirical force models. Xiong *et al.*[22] analyzed settling and floating motion characteristics of a sphere based on the resolved CFD-DEM method. However, research results on the hydraulic collection of coarse particles are rarely reported.

The hydraulic collection has a particular impact on the marine environment. Oebius *et al.*[36] simulated the impact of deep-sea mining on the marine environment through a large number of experiments and established numerical forecast models to predict some parameters of sediment particle behavior. The dispersion and resettlement of nodule particles in deep-sea mining areas were simulated by Rolinski *et al.*[37] They found the dispersion and resettlement of nodule particles depend largely on the distribution of particle size. Grupe *et al.*[38] investigated the relations between primitive soil mechanical properties and various physical parameters before mining, such as particle size distribution, and mineral composition. Finally, they predicted the pickup vehicle would sink 15–20 cm into the seabed. Subsequently, a large number of researchers made some surveys and predictions, but the actual impact needed to be tested in future practice.[39–41] To better develop the marine nodule minerals and reduce their impact on the marine environment in the future, now it is necessary to know the motion and mechanical characteristics of coarse particles during hydraulic collection and give appropriate collection parameters to improve the efficiency of hydraulic collection and protect the environment.

The FDM is implemented based on the computational fluid dynamics/discrete element (CFDEM),[42,43] which is divided into the Open Field Operation and Manipulation (OpenFOAM) for CFD part and the LAMMPS improved for general granular and granular heat transfer simulations (LIGGGHTS) for DEM part.[44] The OpenFOAM solves the flow field, and the particle information is obtained through the LIGGGHTS, which can significantly improve computational efficiency. In addition, the dynamic mesh model of the FDM can automatically refine the meshes occupied by particles, avoiding the initial large number of fine meshes to increase computation. Thus, this paper adopts the FDM based on the CFDEM to study the hydraulic collection.

The aim of the paper is to investigate the motion and mechanical characteristics of coarse particles during hydraulic collection by using the FDM. First, the motion and normalized particle–fluid interaction force characteristics of the particle rise are investigated during the hydraulic collection. It is worth noting that the fluid–particle interaction force is the fluid drag force in the FDM.[32] Second, the effects of different particle sizes and fluid velocities on the normalized fluid drag force and the particle rise time are analyzed. Additionally, the influence of the horizontal distance between particles and the pipe inlet on the particle rise is discussed. In Sec. II, the governing equation of the resolved CFD-DEM (FDM) is carefully introduced. Section III is the computational model and conditions. Section IV is the validation of FDM and numerical results. Finally, Sec. V summarizes the research results of the paper.

II. RESOLVED CFD-DEM METHODS

A. Discrete phase equations

The motion information of a solid particle is obtained by solving the momentum and angular momentum equations of a single particle. They are as follows:[45,46]

$$m_{\mathrm{p}} \frac{\mathrm{d}\mathbf{u}_{\mathrm{p}}}{\mathrm{d}t} = \mathbf{F}_{\mathrm{fp}} + \sum_{j \neq i}^{N_{\mathrm{p}}} \mathbf{F}_{\mathrm{c,ij}} + \sum_{k \neq i}^{N_{\mathrm{w}}} \mathbf{F}_{\mathrm{c,ik}} + m_{\mathrm{p}}\mathbf{g}, \tag{1}$$

$$I_{\mathrm{p}} \frac{\mathrm{d}\boldsymbol{\omega}_{\mathrm{p}}}{\mathrm{d}t} = \sum_{j \neq i}^{N_{\mathrm{p}}} \mathbf{T}_{\mathrm{c,ij}} + \sum_{k \neq i}^{N_{\mathrm{w}}} \mathbf{T}_{\mathrm{c,ik}}, \tag{2}$$

where m_{p} and $\mathbf{u}_{\mathrm{p}}$ are the particle mass and particle velocity, $\mathbf{F}_{\mathrm{fp}}$ is the fluid drag force, $\mathbf{g}$ is the acceleration of gravity, $\mathbf{F}_{\mathrm{c,ij}}$ is the collision force between particle i and particle j, $\mathbf{F}_{\mathrm{c,ik}}$ is the collision force between particle i and wall k, I_{p} and $\boldsymbol{\omega}_{\mathrm{p}}$ are the moment of inertia and the angular velocity of the particle, and $\mathbf{T}_{\mathrm{c,ij}}$ and $\mathbf{T}_{\mathrm{c,ik}}$ are the torque at particle–particle and particle–wall collisions, respectively.

In this paper, for one thing, we mainly study the hydraulic collection of a single coarse particle; for another thing, because the diameter of the geometric model is large enough, the influence of the wall on a single coarse particle motion can be ignored. Thus, the particle–particle/wall collision can be ignored.

B. Continuous phase equations

Figure 2(a) shows a sketch of fluid domain Ω_{f} and particle domain Ω_{p}. Ω is the whole domain ($\Omega = \Omega_{\mathrm{f}} + \Omega_{\mathrm{p}}$). Γ and Γ_{s} are the fluid boundary and interface between fluid and solid particles, respectively. Figure 2(b) shows the fluid meshes are occupied by a particle and the interface (Γ_{s}) between the particle and fluid is refined by the dynamic mesh model of the FDM.

The flow field information is obtained based on the Euler method by solving mass and momentum conservation equations of incompressible fluid[47,48]

$$\nabla \cdot \mathbf{u}_{\mathrm{f}} = 0 \quad \text{in}\ \Omega_{\mathrm{f}}, \tag{3}$$

$$\frac{\partial \mathbf{u}_{\mathrm{f}}}{\partial t} + \nabla \cdot (\mathbf{u}_{\mathrm{f}}\mathbf{u}_{\mathrm{f}}) = \frac{\nabla P}{\rho_{\mathrm{f}}} + \mu_{\mathrm{f}} \nabla^2 \mathbf{u}_{\mathrm{f}} \quad \text{in}\ \Omega_{\mathrm{f}}. \tag{4}$$

The initial conditions are given as follows:

$$\mathbf{u}_{\mathrm{f}}(\mathbf{x}, t = 0) = \mathbf{u}_0(\mathbf{x}) \quad \text{in}\ \Omega_{\mathrm{f}}. \tag{5}$$

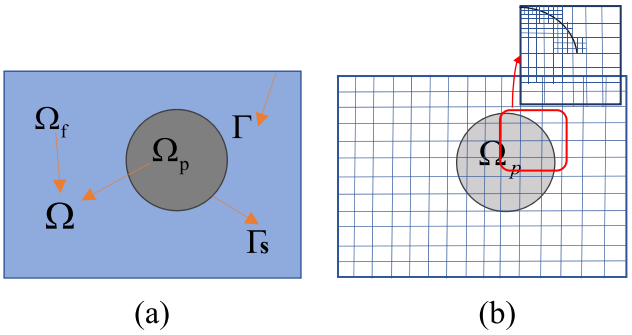

FIG. 2. Resolved CFD-DEM method: (a) sketch of the whole domain and (b) mesh refinement.

The boundary conditions are given as follows:

$$\mathbf{u}_{\mathrm{f}} = \mathbf{u}_{\Gamma} \quad \text{on}\ \Gamma. \tag{6}$$

The conditions at the solid–fluid interface Γ_{s} are given by Eqs. (7) and (8) as follows:

$$\mathbf{u}_{\mathrm{f}} = \mathbf{u}_{\mathrm{p}} \quad \text{on}\ \Gamma_{\mathrm{s}}, \tag{7}$$

$$\boldsymbol{\sigma} \cdot \vec{n} = \vec{t} \quad \text{on}\ \Gamma_{\mathrm{s}}, \tag{8}$$

where $\mathbf{u}_{\mathrm{f}}$, $\mathbf{u}_{\mathrm{p}}$, $\mathbf{u}_0$, and $\mathbf{u}_{\Gamma}$ are the fluid velocity, the particle velocity, the fluid velocity of initial conditions, and the fluid velocity of the interface between the particle and fluid, respectively; ρ_{f} is the fluid density; μ_{f} is the kinematic viscosity of fluid; $\boldsymbol{\sigma}$ is the stress tensor; $\vec{n}$ is the outer normal vector of the particle surface; and $\vec{t}$ is the traction vector of the fluid acting on the particle.

C. Drag force calculation

Equations (7) and (8) are responsible for the coupling of the solid–fluid two phases.[32,49] Equation (7) matches the no-slip boundary condition. Equation (8) is used to calculate the fluid stress acting on solid particles, and the stress can be transformed to Eq. (1).

Equation (8) is integrated on the interface between the particle and fluid (Γ_{s})

$$\int_{\Gamma_{\mathrm{s}}} \boldsymbol{\sigma} \cdot \vec{n}\, d\Gamma_{\mathrm{s}} = \int_{\Gamma_{\mathrm{s}}} \vec{t}\, d\Gamma_{\mathrm{s}}, \tag{9}$$

where $\vec{n}$ is the outer normal vector of the particle, and it points from fluid to particle surface.[32,50] $\boldsymbol{\sigma}$ is the stress tensor, And $\vec{t}$ is the traction vector of the fluid acting on the particle.

The divergence theorem yields

$$\int_{\Omega_{\mathrm{p}}} \nabla \cdot \boldsymbol{\sigma}\, d\Omega_{\mathrm{p}} = \int_{\Gamma_{\mathrm{s}}} \vec{t}\, d\Gamma_{\mathrm{s}}. \tag{10}$$

The fluid is an incompressible and Newtonian fluid, which causes the relation

$$\boldsymbol{\sigma} = -p\mathbf{I} + \boldsymbol{\tau}_{\mathrm{f}}, \tag{11}$$

$$\boldsymbol{\tau}_{\mathrm{f}} = \mu_{\mathrm{f}} \left(\nabla \mathbf{u}_{\mathrm{f}} + \nabla \mathbf{u}_{\mathrm{f}}^{\mathrm{T}}\right), \tag{12}$$

where $\boldsymbol{\tau}_{\mathrm{f}}$ is the viscous stress tensor of the fluid, $\mathbf{I}$ is the unit matrix, and μ_{f} is the coefficient of fluid viscosity.

As a consequence, Eq. (10) can be changed to Eq. (13)

$$\int_{\Omega_p} -\nabla p + \nabla \cdot \left(\boldsymbol{\mu}_f\left(\nabla \mathbf{u}_f + \nabla \mathbf{u}_f^T\right)\right) d\Omega_p = \int_{\Gamma_s} \vec{t}\, d\Gamma_s. \tag{13}$$

Because $\nabla \cdot \mathbf{u} = 0$, the force is given as follows:

$$\int_{\Gamma_s} \vec{t}\, d\Gamma_s = \int_{\Omega_p} -\nabla p + \mu_f \nabla^2 \mathbf{u}_f\, d\Omega_p. \tag{14}$$

If the integral is extended over the whole domain (Ω), Eq. (14) becomes Eq. (15)

$$\int_{\Omega_p} \left(-\nabla p + \mu_f \nabla^2 \mathbf{u}_f\right)\varepsilon_c\, d\Omega = \sum_{c \in V_{\Omega_p}} \int_{V_c} \left(-\nabla P + \mu_f \nabla^2 \mathbf{u}_f\right)\varepsilon_c\, dV_c, \tag{15}$$

where ε_c is 1 in the Ωp; otherwise, ε_c is 0. V_{Ω_p} is cells covered by solid particle, and V_c denotes the volume of cell c.

The velocity for the force is obtained by weighting the void fraction of the interface between fluid and solid

$$\mathbf{u}_f = \tilde{\mathbf{u}}_f \alpha_f + \mathbf{u}_p(1 - \alpha_f), \tag{16}$$

where $\tilde{\mathbf{u}}_f$ is the corrected fluid velocity at the last time step, α_f is the volume fraction of the fluid, and $(1 - \alpha_f)$ is the volume fraction of solid particles. The details of the method for computing the void fraction can be found in Refs. 32 and 49.

Finally, the fluid drag force is obtained by Eq. (17) as follows:

$$\mathbf{F}_{fp} = \sum_{c \in V_{\Omega_p}} \left(-\nabla P + \mu_f \nabla^2 \mathbf{u}_f\right)_c V_c, \tag{17}$$

where $\mathbf{F}_{fp}$ is the fluid drag force.

D. Algorithm of cfdemSolverIB solver

The FDM based on the CFDEM platform is developed into the "cfdemSolverIB" solver.[42,43] As shown in Fig. 3, the cfdemSolverIB solver consists of three modules: the DEM module, the CFD module, and the coupling module. The solver mainly has the following algorithm:[51,52]

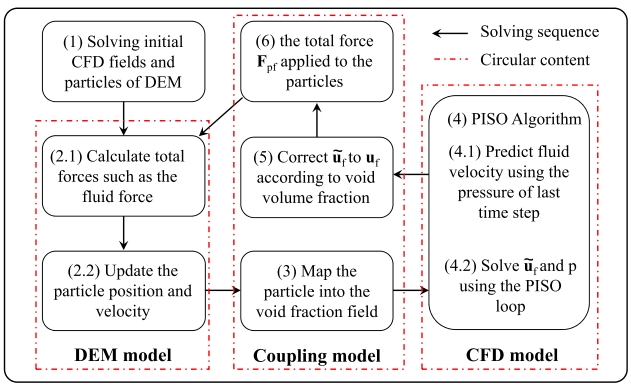

FIG. 3. Flow chart of the cfdemSolverIB solver.

(1) Solve the position and velocity of particles within a specific time step based on the LIGGGHTS platform and pass these values to OpenFOAM.
(2) The void fraction model identifies particles and fluid meshes occupied by particles. Then, the dynamical mesh model of the FDM refines these meshes.
(3) The flow field information is calculated when the presence of particles is not considered. Then, the particle velocity is corrected in meshes covered by particles.
(4) The force of fluid acting on the particles is solved by Eq. (17) and passed to LIGGGHTS.
(5) The flow field information is corrected to satisfy the mass conservation equation.
(6) The fluid pressure is corrected, and the next time step cycle begins.

For the cfdemSolverIB solver, the void fraction of the mixture of particles and fluid is mapped onto the background mesh. Then, the volume fraction is calculated according to the volume of the particles occupying the meshes. The details of the method for computing the void fraction can be found in Refs. 32 and 49.

III. NUMERICAL SETUP

As shown in Fig. 4(a), the geometry is formed in a cylinder with a diameter of 200 mm and a height of 60 mm. Figure 4(a) is the main view. Compared with the diameter of the particles, the diameter of the cylinder is large enough to reduce the influence of the wall on the particle motion. The calculation domain is divided into approximately uniform hexahedral meshes with about 150 000 cells. As shown in Fig. 4(b), meshes of the flow field occupied by the particle are refined by the dynamic mesh model. The computational domain has five boundaries: Inlet, top, bottom, pipewall, and wall. The suction inlet is set at 30 mm (3 d_p) from the bottom. At the inlet, a fixed value is set for the fluid velocity, and a zero gradient is defined for the fluid pressure. Pressure out boundary condition is set at the top. The bottom, pipewall, and wall are specified to be zero for the fluid velocity and zero gradients for the pressure.[19,50] It is worth noting that we only focus on the particle rise before the particles enter the inlet, and the movement of the particles in the pipe is our other research topic.[53]

The particle size is $d_p = 10$ mm with the density $\rho_p = 2450$ kg/m^3, and the particle is a standard sphere. The fluid default is room temperature water with a density of $\rho_f = 1000$ kg/m^3 and a viscosity of $\mu_f = 0.001$ kg/(m s). In the initial conditions, the particle is stationary at the bottom. Then, the particle is sucked from the inlet of the pipe under the action of a pre-set fixed fluid velocity. The fluid

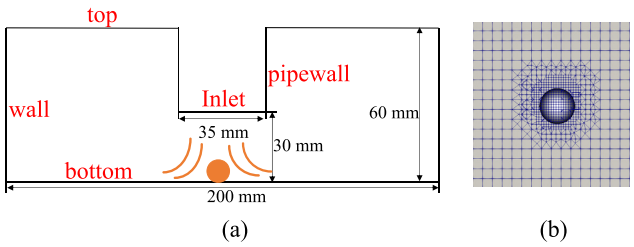

FIG. 4. Computational geometry: (a) main view and (b) the refinement of the dynamic mesh model.

TABLE I. Parameters are used in the numerical simulation of hydraulic collection.[10,54]

Parameters	Values
Particle properties	
Density, ρ_p	2450 kg/m^3
Diameter, d_p	10–15 mm
Young's modulus, E	1.0 $\times 10^8$ Pa
Poisson's ratio, ν	0.23
Water properties	
Density, ρ_f	1000 kg/m^3
Viscosity, μ_f	1.0 $\times$ 10^{-3} Pa s
Velocity, $\mathbf{u}_0$	1.3–1.8 m/s
Fluid temperature	25 °C
Simulation setup	
CFD time step	5.0 $\times$ 10^{-4} s
DEM time step	1.0 $\times$ 10^{-5} s
Simulation time	5 s

velocities range from 1.3 to 1.8 m/s, and the particle diameter varies from 10 to 15 mm. The parameters of the numerical simulation are shown in Table I. In this paper, the effects of different particle sizes and fluid velocities on the hydraulic collection of coarse particles are analyzed. The influence of different horizontal distances between particles and the inlet on particle rise is also discussed, which can be used to determine the range of the horizontal distance that the particles can be sucked and the optimal range.

According to the FDM algorithm, the DEM for solving particle motion is different from the CFD module for solving the flow field. The time steps of DEM (Δt_{DEM}) and CFD (Δt_{CFD}) are generally different. Rayleigh time (Δt_R) is calculated by Li *et al.*[55] and Yang *et al.*[56]

$$\Delta t_R = \frac{\pi R_i}{0.163\nu + 0.8766}\sqrt{\frac{2\rho_p(1+\nu)}{E}}, \tag{18}$$

where R_i is the particle radius, E is Young's Modules, and ν is Poisson's ratio. The time step of the DEM module for solving particle motion should be smaller than the Rayleigh time.[54] Thus, the time step in LIGGGHTS is set to 1.0 $\times$ 10^{-5} s. In the FDM, the time step of the fluid solution is generally 10–100 times the time step of DEM, so the time step in OpenFOAM is set to 5.0 $\times$ 10^{-4} s.

IV. RESULTS AND DISCUSSION

A. Model validation

In this part, the FDM is verified by comparing the particle falling velocity freely in the pipe between numerical and theoretical results. First, a cylindrical pipe with a diameter of 200 mm and a height of 1.2 m is formed. Second, the particle sizes are 10, 20, 30, 40, and 50 mm, and particle density is $\rho_p = 2450$ kg/m^3. Fluid default is the normal temperature water with a density of $\rho_f = 1000$ kg/m^3 and a viscosity of $\mu_f = 0.001$ kg/(m s). The initial position of the particles is in the middle of the top of the pipe (0, 0, 1). Then, the particle is released freely from the top of the pipe. The velocity is the final settling velocity when the trajectory and velocity of the particle are stable. The theoretical settling velocity of the particle is calculated by Eq. (19)[22]

$$v_p = \sqrt{\frac{4(\rho_p - \rho_f)gd_p}{3C_d\rho_f}}, \tag{19}$$

where C_d is the drag coefficient and v_p is the particle velocity.

The corrected particle settling velocity considering boundary effect is used in this paper:[57]

$$v_p = \left[1 - \left(\frac{d_p}{D}\right)^{1.5}\right]\sqrt{\frac{4(\rho_p - \rho_f)gd_p}{3C_d\rho_f}}, \tag{20}$$

where D is the pipe diameter.

Figure 5(a) is the flow field of the particle falling process. The trajectory and velocity of the particle gradually stabilize as the particle falls. Figure 5(b) shows the comparison of the final settling velocities of different particle sizes between numerical and theoretical results. The numerical results are close to the theoretical results.

When the particle settles in the viscosity fluid, the resistant force is the buoyancy force and the fluid drag force, and the driving force is the gravity. When these three forces are balanced, the particle is in equilibrium. The drag coefficient $C_{d,num}$ at the steady state can be obtained based on numerical results[58,59]

$$C_{d,num} = \frac{4}{3}\frac{\rho_p - \rho_f}{\rho_f}\frac{gd_p}{v_p^2}, \tag{21}$$

where v_p is the final settling velocity of the particle.

$C_{d,exe}$ can be experimentally obtained based on experimental tests by using Eq. (22)[60]

$$C_{d,exp} = \frac{24}{Re_p}\left(1 + 0.15Re_p^{0.681}\right) + \frac{0.407}{1 + \frac{8710}{Re_p}}, \tag{22}$$

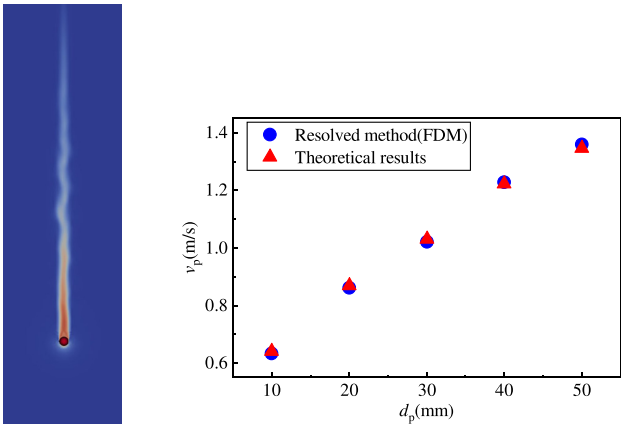

FIG. 5. Comparison of the final settling velocities at different particle sizes: (a) the flow field of the particle falling process freely and (b) the final settling velocities between numerical and theoretical results.

TABLE II. Comparison between experimental and numerical results of single sphere settling.[60]

Case	Box size (L × W × H) (m)	ρ_f(kg/m^3)	μ_f [kg/(m s)]	ρ_p(kg/m^3)	d_p (m)	Numerical results v_p	Re_p	$C_{d,num}$	Experiment, $C_{d,exe}$
1	0.1 × 0.1 × 1	1000	1.19	2000	0.01	0.025	0.21	118.26	117.94
2	0.1 × 0.1 × 1	1260	1.19	2000	0.01	0.042	0.36	72.49	72.24
3	0.1 × 0.1 × 1	1260	1.19	2500	0.01	0.062	0.52	50.38	50.40
4	0.01 × 0.01 × 0.02	1000	0.001	1287.5	0.001	0.048	48.22	1.63	1.54
5	0.01 × 0.01 × 0.02	1000	0.001	1500	0.001	0.068	68	1.39	1.31
6	0.02 × 0.02 × 0.04	1000	0.001	2000	0.001	0.136	272	0.71	0.70

where $Re_p = \frac{v_p d_p}{\nu_f}$ is the particle Reynolds number and ν_f is the coefficient of fluid viscosity.

We summarize six cases to validate the drag coefficients of single sphere settling by comparing the experimental and numerical results in Table II. These cases obtain different particle Reynolds numbers Re_p and the numerical drag coefficient $C_{d,num}$ by changing different material properties. When the fluid is of high viscosity, such as olive oil in cases 1–3, Re_p values are smaller. The fluid is water in cases 4–6, so the Re_p values are larger. The diameter of the box is ten times the particle diameter to reduce the effect of the wall on the particle settling, so the particle–particle/wall collision forces can be ignored. The particle is initially located at the top of the pipe and eventually released freely. As shown in Fig. 6, the numerical drag coefficients are close to the experimental results.

B. Motion of the particle

This work investigates the motion and mechanical characteristics of coarse particles during the hydraulic collection at different fluid velocities and particle sizes. The fluid velocities are 1.3, 1.4, 1.5, 1.6, 1.7, and 1.8 m/s, respectively, and normalized to 1, 1.08, 1.15, 1.23, 1.31, and 1.38 by the fluid velocity of 1.3 m/s. The particle sizes are 10, 11, 12, 13, 14, and 15 mm, respectively, and normalized to 1, 1.1, 1.2, 1.3, 1.4, and 1.5 by the particle size of 10 mm (Ref. 10). The ratio of particle diameter to pipe diameter is $d_p/D > 0.29$, belonging to coarse particles.[14] When the fluid velocity is 1.8 m/s and $d_p = 10$ mm, the minimum particle's rise time is about 0.08 s by the numerical calculation mentioned below. To compare the relative magnitude of physical quantities, the rise time of other different particles is normalized by the minimum particle rise time. The fluid velocity, particle size, and particle's rise time mentioned below are normalized.

This part qualitatively analyzes the motion characteristics of coarse particles by combining the particle trajectory with the qualitative force analysis during the hydraulic collection. The coarse particle is mainly affected by the gravity, the buoyancy force, and the fluid drag force, and these three forces are balanced under critical conditions:

$$\mathbf{F}_{fp} + \mathbf{F}_B + \mathbf{F}_G = 0, \tag{23}$$

$$\mathbf{F}_G = \frac{\pi}{6}\rho_p d_p^3 \mathbf{g}, \quad \mathbf{F}_B = -\frac{\pi}{6}\rho_f d_p^3 \mathbf{g}, \tag{24}$$

where $\mathbf{F}_{fp}$ is the fluid drag force, $\mathbf{F}_B$ is the buoyancy force, $\mathbf{G}$ is the gravity, and ρ_p, ρ_f, d_p are the particle density, fluid density, and particle diameter, respectively.

The qualitative force analysis provides a clear understanding of the physical state of the particle during hydraulic collection. As shown in Fig. 7(a), the particle is stationary on the seabed in the initial condition and subject to the relative gravity (the particle gravity minus the buoyancy) and seabed support force $\mathbf{F}_h$. The relative gravity is $\mathbf{f}_{\tilde{g}} = \mathbf{G} - \mathbf{F}_B$. As the inlet fluid velocity of the suction pipe increases, an upward flow field is formed below the inlet, and the particle begins to fluctuate but does not rise. In this case, the particle is subjected to the fluid drag force and the relative gravity. As shown in Eq. (23), the particle is in a critical rise state when the two forces are equal. When the fluid drag force is greater than the relative gravity, the particle begins to be sucked in Fig. 7(b).

Figure 8 shows the change in particle velocity during hydraulic collection. The normalized fluid velocity and particle size are 1.15 and

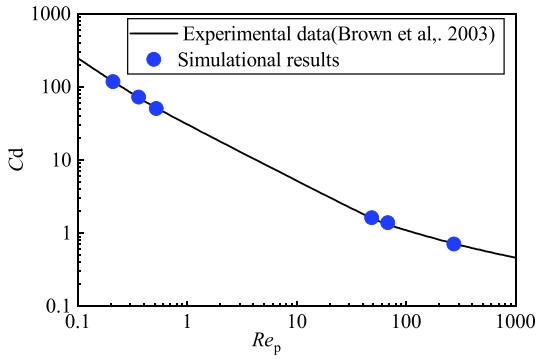

FIG. 6. Drag coefficient of experimental and numerical results at the steady state.

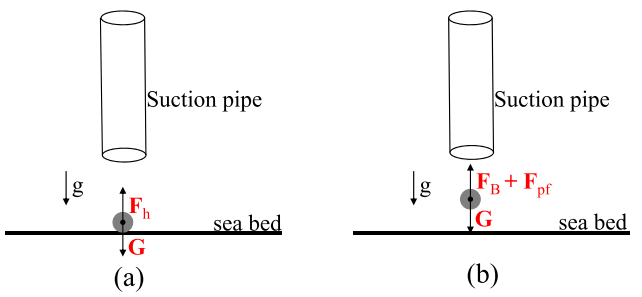

FIG. 7. Qualitative force analysis of the particle: (a) stationary on the seabed and (b) the process of particle rise.

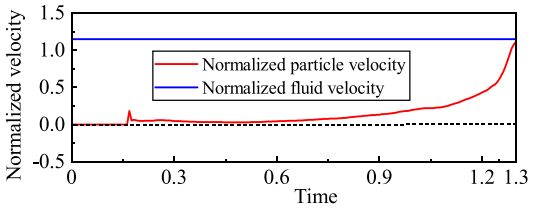

FIG. 8. Variation of the particle velocity during the hydraulic collection.

1, respectively. The normalized fluid velocity and particle size are randomly selected. Since the hydraulic collection of the particle mainly occurs on the z axis, we only consider the variation of particle velocity in the z axis. The z axis upward is positive. As shown in Fig. 8, the particles are initially stationary on the ocean bed, so the particle velocity is 0. In this stage, the relative gravity is greater than the fluid drag force. The particle is in a critical state at around t = 0.15. Then, as the particle velocity is greater than 0, the particle begins to rise. There is a sudden change in particle velocity at around t = 0.17, which is because the instability of the flow field at around t = 0.17 leads to the instability of the fluid drag force. As is shown in Fig. 11, the change of the normalized centripetal force indicates the flow field is expanding and unstable at around t = 0.17, which eventually causes the change of particle velocity.

Figure 9 shows the numerical trajectories of particle rise at the normalized particle size of 1. The spiral phenomenon of the particle is also found in our previous experiments.[10] The numerical results are in good agreement with the experimental results. The particle trajectory corresponds to the change of the particle velocity in Fig. 8. The particle rising process is shown in Fig. 10 (multimedia view).

The spiral phenomenon of the particle is essentially the irregular circular motion of particles. To further explain the phenomenon, we count the components of the fluid drag force with time in the x, y, and z directions when the particles rise at the fluid velocity of 1.15 and the particle size of 1, namely, $\mathbf{F}_{fp'x}$, $\mathbf{F}_{fp'y}$, and $\mathbf{F}_{fp'z}$, respectively. Then, we calculate the resultant force of $\mathbf{F}_{fp'x}$ and $\mathbf{F}_{fp'y}$, named the centripetal force $\mathbf{F}_{cen}$. The centripetal force $\mathbf{F}_{cen}$ can make the particles show irregular circular motion in the x-y plane, and $\mathbf{F}_{fp'z}$ mainly makes particles rise in the z axis. We normalize the centripetal force $\mathbf{F}_{cen}$ by $\mathbf{F}_{fp'z}$, named the normalize centripetal force. As is shown in Fig. 11, the normalized centripetal force $\mathbf{F}_{cen}$ fluctuates around 0.15 at other times

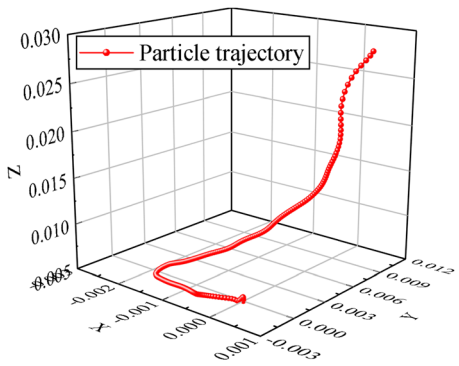

FIG. 9. Trajectory of the particle rise at the normalized particle size of 1.

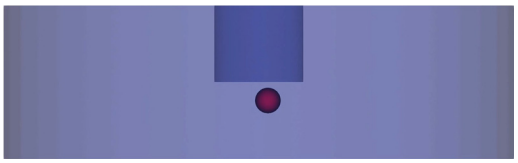

FIG. 10. Particle rising process at the normalized fluid velocity of 1.15 and particle size of 1. Multimedia view: https://doi.org/10.1063/5.0142221.1

except for a sudden change at around t = 0.17. Thus, we believe that centripetal force $\mathbf{F}_{cen}$ is the reason for the irregular circular motion of the particle, that is, the spiral phenomenon of the particle.

C. Force analysis of the particle

This section mainly analyzes the forces and rise time of particles during the hydraulic collection at different fluid velocities and particle sizes. The fluid drag force $\mathbf{F}_{fp}$ and the relative gravity $\mathbf{f}_{\tilde{g}}$ are obtained from numerical results. Because the particle rise mainly occurs on the z axis, the components of two forces on the z axis are considered. To compare the fluid drag force with the relative gravity, the fluid drag force is normalized by the relative gravity. The fluid velocity, particle size, and particle's rise time mentioned above have been normalized.

First, the variation of the average normalized fluid drag force with time is analyzed at the normalized fluid velocities of 1 and 1.08. It is worth noting that the normalized particle size is 1.3 when the velocity changes. As shown in Fig. 12(a), when the normalized fluid velocity is 1, the normalized fluid drag force is less than 1 all the time, which implies that the particle does not rise. While the normalized fluid velocity is 1.08 in Fig. 12(b), the normalized fluid drag force is only less than 1 in the initial stage. In the state, the particle moves on the bottom without rising. Subsequently, when the fluid drag force is greater than the relative gravity (the normalized fluid drag force is greater than 1), the particle begins to rise, corresponding to the particle trajectory of Fig. 9.

Second, the variation of the average normalized fluid drag force and the rise time of particles at different fluid velocities are analyzed. It is also worth noting that the normalized particle size is 1.3 when the velocity changes. As shown in Fig. 13, the normalized fluid drag force is less than 1 at the normalized fluid velocity of 1. The particle cannot be sucked in the state, which is also why there is no rise time of the particle at the normalized fluid velocity of 1 in Fig. 13. The normalized fluid drag force is less than 1; that is, the fluid drag force is less than the relative gravity, so the particle fails to be sucked. While the normalized fluid velocity is greater than 1, the force is greater than 1. The fluid drag force dominates in the case, and the particle successfully rises. Therefore, the rise of particles during hydraulic collection results from

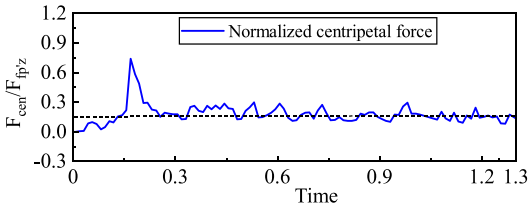

FIG. 11. Change of the normalized centripetal force with time.

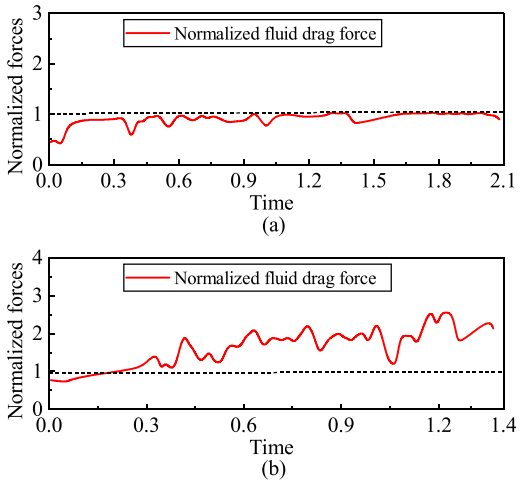

FIG. 12. Variation of average normalized fluid drag force at different normalized fluid velocities: (a) 1 and (b) 1.08.

competition between the fluid drag force and the relative gravity. Our results are consistent with the results of rising and settling effects characterized by the Reynolds number (*Re*) and the Archimedes number (*Ar*) in the experiments.[10]

As the fluid velocity increases, the normalized fluid drag force becomes greater, and the rise time of the particle becomes shorter in Fig. 13. Although shortening the rise time of particles can improve the efficiency of hydraulic collection, it requires more energy to increase fluid velocity, which can result in greater economic costs and have a greater impact on the marine environment. It is irrational to blindly increase the fluid velocity to increase the normalized fluid drag and thus shorten the particle rise time. Therefore, we should choose the appropriate fluid velocity range to save energy and improve efficiency; that is, it is necessary to balance normalized fluid drag force and the rise time of particles in the hydraulic collection. We hope to further study the appropriate fluid velocity range under different working conditions through experiments and field practice in the future.

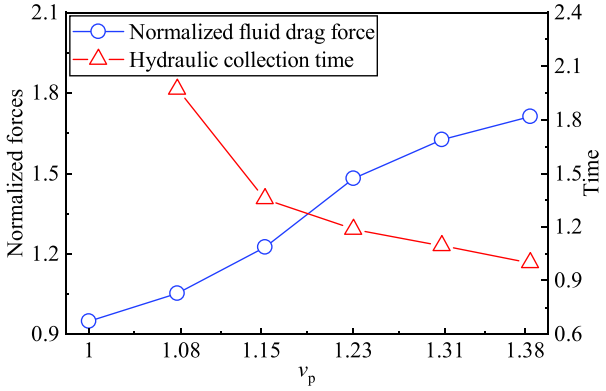

FIG. 13. Normalized fluid drag force and the particle rising time at different normalized fluid velocities: the blue line represents the normalized fluid drag force (left) and the red line represents the rise time of the particle (right).

Finally, we investigate the change of average normalized fluid drag force and rise time of particles by changing different particle sizes. It is worth noting that the fluid velocity of 1.15 is selected when the particle size changes. As shown in Fig. 14, the normalized fluid drag force is both greater than 1, that is, fluid drag force dominants and particle rise. Moreover, the normalized particle size of 1.3 is the turning point. When the normalized particle size is not greater than 1.3 in Fig. 14, the normalized fluid drag force becomes larger as the particle size increases, and the particle rise time becomes shorter. While the normalized particle size is greater than 1.3, the normalized fluid drag force becomes smaller with the increase in particle size, and the time to rise becomes longer. The vertical distance between the particle and the inlet becomes smaller with the increase in particle size, which should have made the particles easily to be sucked. In fact, an increase in the particle size can bring greater gravity, which leads to smaller normalized fluid drag force and much longer rise time of the particle at the particle sizes of 1.4 and 1.5 in Fig. 14. The maximum normalized fluid drag force and the shortest particle rise time are what we want. Thus, the normalized particle size of 1.3 is recommended to save energy and improve efficiency.

D. Analysis of horizontal distance

We find it appropriate that the vertical distance between the particles at the bottom and the inlet of the suction pipe is not greater than 3 d_p in our previous work.[10] The horizontal distance between particles and the inlet of the suction pipe is rarely considered. Thus, it is necessary to discuss the influence of different horizontal distances. In previous cases, the particles were placed below the center of the suction pipe. In this part, we investigate the change of the normalized fluid drag force by changing the horizontal distance between particles and the inlet to determine the range of the horizontal distance that the particles can be sucked and the optimal range. The radius of the pipe is 1.75 d_p.

As shown in Fig. 15, we set the horizontal distance between the particles and the inlet to 1 d_p, 1.75 d_p, 3 d_p, 5 d_p, 7 d_p, and 9 d_p, which is normalized to 1, 1.75, 3, 5, 7, and 9 by particle diameter d_p. In this part, the normalized particle size and fluid velocity are 1.3 and 1.15, respectively. When these particles are sucked at different horizontal distances, we calculate their average normalized fluid drag force in Fig. 16.

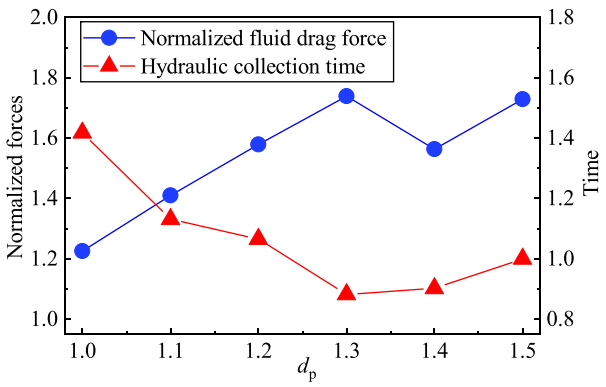

FIG. 14. Normalized fluid drag force and the particle rising time at different normalized particle sizes: the blue line represents the normalized fluid drag force (left), and the red line represents the rise time of the particle (right).

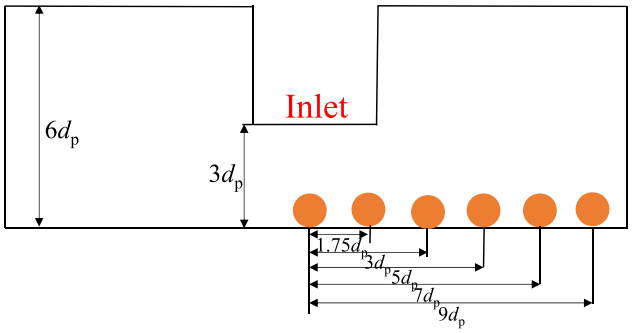

FIG. 15. Horizontal distance between particles and the inlet of the suction pipe.

If the normalized fluid drag force is 1, the particle is in a critical state. While the normalized fluid drag force is greater than 1, the particle begins to rise. When the normalized distances are 1, 1.75, 3, 5, and 7, the normalized fluid drag forces are all greater than 1; that is, these particles can be sucked smoothly. As the horizontal distance becomes larger, the normalized fluid drag force generally becomes smaller in Fig. 16. The normalized fluid drag force is less than 1 at the normalized distance of 9 so that the particle does not rise. Thus, the range of normalized horizontal distance that the particles can be sucked is no more than 8 at the fluid velocity of 1.15 and particle size of 1.3. Of course, increasing the fluid velocity and reducing the particle size can expand the range of the horizontal distance of the particle rise. However, these measures will bring energy loss and economic costs. In addition, it is worth noticing that the normalized fluid drag force at the normalized horizontal distance of 1.75 is larger than that at the distance of 1. The particle is located below the center of the inlet when the normalized distance is 1, and the particle is located below between the inlet and the wall at the normalized distance of 1.75. As a consequence, when the fluid velocity of the inlet is constant, the particles located between the inlet and the wall are more easily sucked. Therefore, the suction influence range between the inlet and wall is more optimized. Compared with fixed collection devices, mobile devices for hydraulic collection are recommended to make particles place below between the inlet and wall, which indicates a mobile suction device is needed.

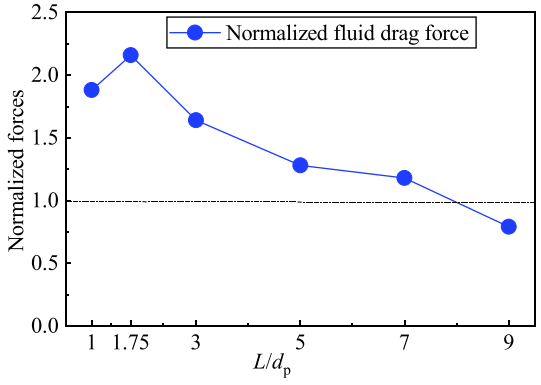

FIG. 16. Variation of average normalized fluid drag force at different horizontal distances and L is the horizontal distance between particles and the inlet.

In summary, the rising process of coarse particles during the hydraulic collection is qualitatively analyzed. The spiral phenomenon of the coarse particle rise is found and explained from the perspective of force analysis. Moreover, the changes in normalized fluid drag force and particle rise time are investigated at different normalized fluid velocities and particle sizes. Finally, the influence of the horizontal distance between the coarse particle and the inlet on particle rise is discussed.

V. CONCLUSION

In this paper, the FDM based on the CFDEM platform is used to study the motion and mechanical characteristics of coarse particles during hydraulic collection, and the influence of the horizontal distance between particles and the inlet on the hydraulic collection of coarse particles is also considered.

(i) First, the motion characteristics of coarse particles during hydraulic collection are analyzed. The changes in particle velocity, trajectory, and qualitative force analysis are consistent during hydraulic collection. The spiral phenomenon of the coarse particle is found in numerical results and in good agreement with our previous experimental results.[10] The numerical results show that the centripetal force $\mathbf{F}_{cen}$ causes the spiral phenomenon of the particle during hydraulic collection.

(ii) Second, the changes in the normalized fluid drag force and the rise time of particles are investigated at different fluid velocities and particle sizes. The results show that the rise of particles during hydraulic collection results from competition between the fluid drag force and the relative gravity. As the normalized particle size and fluid velocity increase, respectively, the normalized fluid drag force generally increases. However, gravity plays a dominant role after the normalized particle size increases to 1.3. To save energy and improve efficiency, the normalized particle size of 1.3 is recommended.

(iii) Finally, we investigate the influence of different horizontal distances between the particles and the inlet on the hydraulic collection of coarse particles. The results show that the influence range of the flow field is limited, and the normalized fluid drag force generally decreases with the increase of horizontal distance. Otherwise, a greater fluid velocity is required. Moreover, the range of normalized horizontal distance that the particles can be sucked is no more than 8 at the fluid velocity of 1.15 and particle size of 1.3, and the suction influence range between the inlet and the wall is more optimized. Thus, mobile collection devices are recommended to make particles placed below the inlet and wall during hydraulic collection.

ACKNOWLEDGMENTS

This work was supported by the National Natural Science Foundation of China (Grant No. 12132018), the Strategic Priority Research Program of the Chinese Academy of Sciences (Grant No. XDA22000000), and the Youth Innovation Promotion Association of Chinese Academy of Sciences (No. 2017027).

AUTHOR DECLARATIONS

Conflict of Interest

The authors have no conflicts to disclose.

Author Contributions

Wanlong Ren: Conceptualization (equal); Investigation (equal); Methodology (lead); Writing – original draft (lead); Writing – review & editing (equal). **Xuhui Zhang:** Funding acquisition (lead); Resources (equal); Supervision (equal); Writing – review & editing (equal). **Yan Zhang:** Conceptualization (equal); Methodology (equal); Software (equal); Supervision (equal); Validation (equal); Writing – review & editing (equal). **Xiaobing Lu:** Funding acquisition (equal); Resources (equal); Supervision (equal); Validation (equal); Writing – review & editing (equal).

DATA AVAILABILITY

The data that support the findings of this study are available from the corresponding author upon reasonable request.

REFERENCES

[1]J. Van Wijk, A. Talmon, and C. van Rhee, "Stability of vertical hydraulic transport processes for deep ocean mining: An experimental study," Ocean Eng. **125**, 203–213 (2016).

[2]Q. Kang, S. Song, J. Yu, B. Shi, Y. Chen, X. Lv, Y. Liu, Z. Bai, B. Hong, W. Wang *et al.*, "Simulation of upward gas-hydrate slurry multiphase flow in a vertical concentric annulus for natural gas hydrate solid fluidization exploitation," Phys. Fluids **33**, 103102 (2021).

[3]T. Tran-Duc, N. Phan-Thien, and B. C. Khoo, "A three-dimensional smoothed particle hydrodynamics dispersion simulation of polydispersed sediment on the seafloor using a message passing interface algorithm," Phys. Fluids **31**, 043301 (2019).

[4]W. Chen, H.-L. Xu, F.-Q. Yang, X. Rao, Y.-X. Zhou, D. Hu, and L. Peng, "Research on the transportation and flow characteristics of deep-sea ore transportation equipment," Appl. Ocean Res. **113**, 102765 (2021).

[5]Y. Kang and S. Liu, "The development history and latest progress of deep-sea polymetallic nodule mining technology," Minerals **11**, 1132 (2021).

[6]S. Hong, J.-S. Choi, J.-H. Kim, and C.-K. Yang, "A note on design and operation of waterjet nodule lifter of manganese nodule collector," Int. J. Offshore Polar Eng. **11**, 237–239 (2001); available at https://www.webofscience.com/wos/alldb/full-record/WOS:000170880600012.

[7]N. Yang and H. Tang, "Several considerations of the design of the hydraulic pick-up device," in *Fifth ISOPE Ocean Mining Symposium* (OnePetro, 2003).

[8]G. Zhao, L. Xiao, T. Peng, and M. Zhang, "Experimental research on hydraulic collecting spherical particles in deep sea mining," Energies **11**, 1938 (2018).

[9]Y. Chen, H. Xiong, H. Cheng *et al.*, "Experimental study on the incipient motion of a single spherical particle in hydraulic collecting," J. Cent. South Univ. **50**, 2831–2838 (2019).

[10]Y. Zhang, X. Lu, X. Zhang, Y. Chen, H. Xiong, and L. Zhang, "Experimental investigation of critical suction velocity of coarse solid particles in hydraulic collecting," Acta Mech. Sin. **37**, 613–619 (2021).

[11]G. Zhao, L. Xiao, Z. Yue, M. Liu, T. Peng, and W. Zhao, "Performance characteristics of nodule pick-up device based on spiral flow principle for deep-sea hydraulic collection," Ocean Eng. **226**, 108818 (2021).

[12]B. Viggiano, O. Skjaeraasen, H. Schümann, M. Tutkun, and R. B. Cal, "Characterization of flow dynamics and reduced-order description of experimental two-phase pipe flow," Int. J. Multiphase Flow **105**, 91–101 (2018).

[13]N. Ali, B. Viggiano, M. Tutkun, and R. B. Cal, "Cluster-based reduced-order descriptions of two phase flows," Chem. Eng. Sci. **222**, 115660 (2020).

[14]F. D. Cúñez, N. C. Lima, and E. M. Franklin, "Motion and clustering of bonded particles in narrow solid–liquid fluidized beds," Phys. Fluids **33**, 023303 (2021).

[15]A. Ozel, Y. Gu, C. C. Milioli, J. Kolehmainen, and S. Sundaresan, "Towards filtered drag force model for non-cohesive and cohesive particle-gas flows," Phys. Fluids **29**, 103308 (2017).

[16]M. H. Kasbaoui, D. L. Koch, and O. Desjardins, "Clustering in Euler–Euler and Euler–Lagrange simulations of unbounded homogeneous particle-laden shear," J. Fluid Mech. **859**, 174–203 (2019).

[17]Y. Dai, Y. Zhang, and X. Li, "Numerical and experimental investigations on pipeline internal solid-liquid mixed fluid for deep ocean mining," Ocean Eng. **220**, 108411 (2021).

[18]T. Lichtenegger and T. Miethlinger, "On the connection between Lagrangian and Eulerian metrics for recurrent particulate flows," Phys. Fluids **32**, 113308 (2020).

[19]Y. Zhang, X.-B. Lu, and X.-H. Zhang, "An optimized Eulerian–Lagrangian method for two-phase flow with coarse particles: Implementation in open-source field operation and manipulation, verification, and validation," Phys. Fluids **33**, 113307 (2021).

[20]Y. Yao, C. S. Criddle, and O. B. Fringer, "Competing flow and collision effects in a monodispersed liquid–solid fluidized bed at a moderate Archimedes number," J. Fluid Mech. **927**, A28 (2021).

[21]H. Li, X. Ku, and J. Lin, "Eulerian–Lagrangian simulation of inertial migration of particles in circular Couette flow," Phys. Fluids **32**, 073308 (2020).

[22]H. Xiong, Y. Chen, N. Yang, J. Xiao, and L. Li, "Numerical study on settling and floating movements of a sphere particle flowing in a vertical pipe," in *The 28th International Ocean and Polar Engineering Conference* (OnePetro, 2018).

[23]W.-L. Ren, Y. Zhang, X.-H. Zhang, and X.-B. Lu, "Investigation of the characteristics and mechanisms of the layer inversion in binary liquid–solid fluidized beds with coarse particles," Phys. Fluids **34**, 103325 (2022).

[24]K. Cheng, Y. Wang, and Q. Yang, "A semi-resolved CFD-DEM model for seepage-induced fine particle migration in gap-graded soils," Comput. Geotech. **100**, 30–51 (2018).

[25]H. Xiao and J. Sun, "Algorithms in a robust hybrid CFD-DEM solver for particle-laden flows," Commun. Comput. Phys. **9**, 297–323 (2011).

[26]X. Zhao, L. Yang, C. Xu, and C. Shu, "An overset boundary condition-enforced immersed boundary method for incompressible flows with large moving boundary domains," Phys. Fluids **34**, 103613 (2022).

[27]Z. Chen, C. Shu, L. Yang, X. Zhao, and N. Liu, "Immersed boundary–simplified thermal lattice Boltzmann method for incompressible thermal flows," Phys. Fluids **32**, 013605 (2020).

[28]A. Hager, *CFD-DEM on Multiple Scales: An Extensive Investigation of Particle–Fluid Interactions* (Johannes Kepler University Linz, Linz, 2014).

[29]A. Hager, C. Kloss, S. Pirker, and C. Goniva, "Parallel resolved open source CFD-DEM: Method, validation and application," J. Comput. Multiphase Flows **6**, 13–27 (2014).

[30]N. A. Patankar, P. Singh, D. D. Joseph, R. Glowinski, and T.-W. Pan, "A new formulation of the distributed Lagrange multiplier/fictitious domain method for particulate flows," Int. J. Multiphase Flow **26**, 1509–1524 (2000).

[31]M. Isoz, M. K. Šourek, O. Studeník, and P. Kočí, "Hybrid fictitious domain-immersed boundary solver coupled with discrete element method for simulations of flows laden with arbitrarily-shaped particles," Comput. Fluids **244**, 105538 (2022).

[32]Z. Shen, G. Wang, D. Huang, and F. Jin, "A resolved CFD-DEM coupling model for modeling two-phase fluids interaction with irregularly shaped particles," J. Comput. Phys. **448**, 110695 (2022).

[33]Z. Yu and X. Shao, "Direct numerical simulation of particulate flows with a fictitious domain method," Int. J. Multiphase Flow **36**, 127–134 (2010).

[34]Z. Wang and M. Liu, "On the determination of grid size/smoothing distance in un-/semi-resolved CFD-DEM simulation of particulate flows," Powder Technol. **394**, 73–82 (2021).

[35]Z. Xie, S. Wang, and Y. Shen, "CFD-DEM study of segregation and mixing characteristics under a bi-disperse solid-liquid fluidised bed," Adv. Powder Technol. **32**, 4078–4095 (2021).

[36]H. U. Oebius, H. J. Becker, S. Rolinski, and J. A. Jankowski, "Parametrization and evaluation of marine environmental impacts produced by deep-sea manganese nodule mining," Deep-Sea Res. Part II **48**, 3453–3467 (2001).

[37]S. Rolinski, J. Segschneider, and J. Sündermann, "Long-term propagation of tailings from deep-sea mining under variable conditions by means of numerical simulations," Deep-Sea Res. Part II **48**, 3469–3485 (2001).

[38]B. Grupe, H. J. Becker, and H. U. Oebius, "Geotechnical and sedimentological investigations of deep-sea sediments from a manganese nodule field of the Peru Basin," Deep-Sea Res. Part II **48**, 3593–3608 (2001).
[39]H. Du, G. Wei, S.-D. Wang, and X.-L. Wang, "Experimental study of elevation- and depression-type internal solitary waves generated by gravity collapse," Phys. Fluids **31**, 102104 (2019).
[40]E. Simon-Lledó, B. J. Bett, V. A. Huvenne, K. Köser, T. Schoening, J. Greinert, and D. O. Jones, "Biological effects 26 years after simulated deep-sea mining," Sci. Rep. **9**, 8040 (2019).
[41]R. Cao, S. Wang, G. Xu, and X. Lv, "Characteristics of liquefied soil motion in wavy environment," Phys. Fluids **31**, 073102 (2019).
[42]R. Berger, C. Kloss, A. Kohlmeyer, and S. Pirker, "Hybrid parallelization of the LIGGGHTS open-source DEM code," Powder Technol. **278**, 234–247 (2015).
[43]J. Mao, L. Zhao, X. Liu, and E. Avital, "A resolved CFDEM method for the interaction between the fluid and the discontinuous solids with large movement," Int. J. Numer. Methods Eng. **121**, 1738–1761 (2020).
[44]M. Jahani, A. Farzanegan, and M. Noaparast, "Investigation of screening performance of banana screens using LIGGGHTS DEM solver," Powder Technol. **283**, 32–47 (2015).
[45]L. Liu, J. Yang, H. Lu, X. Tian, and W. Lu, "Numerical simulations on the motion of a heavy sphere in upward Poiseuille flow," Ocean Eng. **172**, 245–256 (2019).
[46]E. Amani, M. Mehrabian, and S. Movahed, "A discrete phase hybrid continuum-atomistic model for electrokinetics in nanofluidics," Phys. Fluids **30**, 072003 (2018).
[47]S. V. Apte, M. Martin, and N. A. Patankar, "A numerical method for fully resolved simulation (FRS) of rigid particle–flow interactions in complex flows," J. Comput. Phys. **228**, 2712–2738 (2009).
[48]Z. Wang, H. Wang, K. Luo, and J. Fan, "Direct numerical simulation of particle-laden turbulent boundary layers without and with combustion," Phys. Fluids **32**, 105108 (2020).
[49]S. Haeri and J. Shrimpton, "On the application of immersed boundary, fictitious domain and body-conformal mesh methods to many particle multiphase flows," Int. J. Multiphase Flow **40**, 38–55 (2012).
[50]E. A. Schnorr Filho, N. C. Lima, and E. M. Franklin, "Resolved CFD-DEM simulations of the hydraulic conveying of coarse grains through a very-narrow elbow," Powder Technol. **395**, 811–821 (2022).
[51]R. Mohan, S. Sundararaj, and K. B. Thiagarajan, "Numerical simulation of flow over buildings using OpenFOAM®," AIP Conf. Proc. **2112**, 020149 (2019).
[52]E. Johnson, D. Baker, and I. Tari, "Development of view factor correlations for modeling thermal radiation in solid particle solar receivers using CFD-DEM," AIP Conf. Proc. **2126**, 030028 (2019).
[53]Y. Zhang, X.-B. Lu, and X.-H. Zhang, "Numerical simulation on transportation behavior of dense coarse particles in vertical pipe with an optimized Eulerian–Lagrangian method," Phys. Fluids **34**, 033305 (2022).
[54]L. Li, B. Li, and Z. Liu, "Modeling of spout-fluidized beds and investigation of drag closures using OpenFOAM," Powder Technol. **305**, 364–376 (2017).
[55]Y. Li, Y. Xu, and C. Thornton, "A comparison of discrete element simulations and experiments for 'sandpiles' composed of spherical particles," Powder Technol. **160**, 219–228 (2005).
[56]S. Yang, K. Luo, J. Fan, and K. Cen, "Particle-scale investigation of the solid dispersion and residence properties in a 3-D spout-fluid bed," AIChE J. **60**, 2788–2804 (2014).
[57]G. Chen, N. Yang, D. Tang, X. Jin, and H. Xiao, "Study on the settling regularity of solid particles in vertical pipelines," J. Sediment Res. **4**, 16–21 (2010).
[58]R. Glowinski, T.-W. Pan, T. I. Hesla, D. D. Joseph, and J. Periaux, "A fictitious domain approach to the direct numerical simulation of incompressible viscous flow past moving rigid bodies: Application to particulate flow," J. Comput. Phys. **169**, 363–426 (2001).
[59]J. Chen and J. Li, "Prediction of drag coefficient and ultimate settling velocity for high-density spherical particles in a cylindrical pipe," Phys. Fluids **32**, 053303 (2020).
[60]P. P. Brown and D. F. Lawler, "Sphere drag and settling velocity revisited," J. Environ. Eng. **129**, 222–231 (2003).